LAWRENCE
LIVERMORE
NATIONAL
LABORATORY

UCRL-JRNL-213175

Oxidation resistance and microstructure of Ru-capped extreme ultraviolet lithography multilayers

S. Bajt, Z. Dai, E. J. Nelson, M. A. Wall, J. B. Alameda, N. Nguyen, S. L. Baker, J. C. Robinson, J. S. Taylor, A. Aquila, N. V. Edwards

June 23, 2005

Journal of Microlithography, Microfabrication and Microsystems

Oxidation resistance and microstructure of Ru-capped extreme ultraviolet lithography multilayers

Saša Bajt*[a], Zu Rong Dai[a], Erik J. Nelson[a], Mark A. Wall[a], Jennifer B. Alameda[a], Nhan Q. Nguyen[a], Sherry L. Baker[a], Jeffrey C. Robinson[a], John S. Taylor[a], Andrew Aquila[b], and N. V. Edwards[c]

[a]Lawrence Livermore National Laboratory, 7000 East Avenue, Livermore, CA 94550, USA;

[b]Lawrence Berkeley National Laboratory, 1 Cyclotron Road, Berkeley, CA 94720, USA;

[b]SEMATECH, Austin, TX 78741-6499, USA

ABSTRACT

The oxidation resistance of protective capping layers for extreme ultraviolet lithography (EUVL) multilayers depends on their microstructure. Differently prepared Ru-capping layers, deposited on Mo/Si EUVL multilayers, were investigated to establish their baseline structural, optical, and surface properties in as-deposited state. The same capping layer structures were then tested for their thermal stability and oxidation resistance. The best performing Ru-capping layer structure was analyzed in detail with transmission electron microscopy (TEM). As compared to other Ru capping layers preparations studied here it is the only one that shows grains with preferential orientation. This information is essential for modeling and performance optimization of EUVL multilayers.

Keywords: EUVL, multilayer, capping layer, Mo/Si, Ru, microstructure, oxidation, thermal stability

1. INTRODUCTION

EUVL is the leading next generation lithography for semiconductor industry. This technology uses 13.5 nm wavelength light to print features as small as 45 nm and below. Reflection multilayer coatings consisting of alternating pairs of Mo and Si is the single, most important technology that enabled EUVL. However, optics lifetime remains a critical issue for the success of EUVL technology. This is true for both the illuminator [1-3] and the projection optics [4-8] even though they operate in different environments and face different contamination issues. In this paper we are discussing only projection optics lifetime.

Water and hydrocarbons are two major contamination sources that reduce the lifetime of projection optics when exposed to the EUV light. Potential solutions fall into three main categories: control, protection and removal. Controlling the EUVL tool environment seems the most obvious solution but it is very hard to achieve. While proper material selection of all components in the system can definitely minimize the outgassing it is impractical to remove outgassing due to resist from the mask. Removal of water vapor is limited because baking is not allowed due to tight temperature specifications and long pumping is undesired because the tools downtime should be as short as possible. Instead of operating in extremely clean environment, the environment can be modified (e.g. introduction of gases, such as ethanol) to reach an optimum balance between oxidation and carbon growth on the optical surfaces [4]. This method has been demonstrated in the Engineering Test Stand (ETS) tool and a similar approach has been considered for the EUVL α-tool of ASML and Carl Zeiss [8, 9]. Carbon contamination on mirror surfaces irradiated with synchrotron irradiation is a well known problem in synchrotron community and has been first described in detail by Boller et al. [10]. Different ways to remove carbon from EUV multilayer coated optics were proposed and tested with minimal or no change to the original reflectivity [5, 9, 11, 12]. However, because oxygen strongly absorbs EUV light oxygen contamination of mirror surfaces is a serious problem. A small increase in oxide layer thickness (<0.3 nm) leads to an unacceptable (>1%) reflectance loss. The interaction between EUV photons and multilayer material creates secondary electrons in the top layers of the multilayer. The secondary electrons that reach the surface of the multilayer and have sufficient energy to break the bonds in water molecules will create free radicals. These radicals can bond to the top (capping) layer atoms and form oxides on the surface or diffuse into or through the top layer and cause oxidation.

* bajt@llnl.gov; phone 1 925 424 3768; fax 1 925 423 1488

Minimizing oxidation by controlling the environment (reducing water vapor in the system) is limited by temperature constraints, and removing the oxide layer, which growths on expense of the capping layer, leads to a thinner capping layer until all of the capping layer is used up. In addition to above mentioned strategies the oxidation can be minimized with protective capping layers. Extended lifetimes have been reported for ruthenium [6, 7] and carbon capping layers [13, 14]. Recently, promising results were reported on a proprietary capping layer based on 230 hours pulsed source exposures with repeated carbon removal in proprietary EUV tool environment [8]. However, to assess the lifetime of EUV multilayers with a chosen capping layer it is necessary to understand the microstructure of the capping layer and to develop physics-based models to predict reflectance degradation with time. This requires state-of-the-art characterization of the capping layers, accelerated testing to determine the scaling laws and feedback to capping layer design. In this paper we are characterizing the microstructure and texture of the best performing Ru capping layers and discuss the effect of the microstructure on their performance as oxidation protective layers.

2. METHODOLOGY

All samples are based on a standard 50 bilayer Mo/Si multilayer deposited on 100-mm diameter Si (100) super-polished wafers (Fig. 1a). These substrates have typical surface high spatial frequency (HSF) roughness of 0.1 nm or better. The multilayer bilayer thickness (the combined Mo and Si layer thickness) was kept constant for all samples at about 6.94 nm. This period thickness is required for operation of these multilayers at 13.4 nm at near normal incidence. Molybdenum thickness divided by the period thickness, referred as Γ, was kept constant at 0.4. All depositions were performed in a dc-magnetron sputtering system (Mag3) using three or four sputtering sources, depending on the capping layer structure [15].

Five different preparation techniques were used to deposit Ru capping layers on Mo/Si-based EUVL multilayers, also called Multilayer 1. Modifications include power change (Preparation 1), sputtering gas change (Preparation 4, 5 and 6) and material variation (Preparation 7). Mo/Si basic multilayer structure was made the same in all cases using ultra-pure Ar sputtering gas. The Ru capping layer in Preparation 1 was prepared using Ar sputtering gas. Ru capping layers for Preparation 4 and Preparation 5 samples were deposited in Ar:N_2 gas mixtures with different Ar:N_2 ratios.

Preparation 6 capping layer was deposited with pure Ar gas but exposed to pure N_2 environment for about 15 minutes before being removed from the deposition tool. We added carbon in the Ru capping layer of Preparation 7.

These multilayer coatings have been characterized in the as-deposited state using a suite of metrologies to establish their baseline information. Multilayers, and in particular, their capping layer structures were then tested for thermal stability and oxidation resistance. We refer to these tests as screening tests. The main objective was to identify the best candidate for further scaling, parametric and accelerated studies.

Multilayer period thickness and detailed multilayer structure (interface roughness, surface roughness, individual layer thicknesses and densities) were determined using x-ray diffractometer with a Cu K_α source (λ = 0.154 nm) by fitting these data with model calculations. Furthermore, surface high spatial frequency rms roughness was obtained with AFM using 2 x 2 μm^2 scans. A reflectometer, at beamline 6.3.2. (Advanced Light Source, LBNL) was used to measure reflectivity as a function of wavelength and to map the samples for their reflectivity variations at a fixed wavelength [16]. The best performing capping layer was studied with Philips CM300 field emission gun (FEG) transmission electron microscope (TEM) that is equipped with Gatan energy filter (GIF) and Oxford Instruments solid-state energy dispersive X-ray spectrometer at LLNL operating at 300 kV. The lattice resolution of the TEM is better than 0.2 nm. Bright-field and dark-field imaging, electron diffraction, high-resolution imaging and energy-dispersive X-ray spectroscopy were employed for the investigation. All images were recorded using a slow-scan charge-coupled-device (CCD) camera (2048 x 2048 pixels). Thermal testing was performed in vacuum at 100ºC for 1 week and at 200ºC for 30 minutes. The oxidation resistance test was performed using electron beam exposures in a water vapor environment. The exposures were performed in Auger microprobes at Sandia National Laboratories (SNL) and Lawrence Livermore National Laboratory (LLNL) using a focused electron beam of 1 keV electrons, which was rastered over about 0.6 x 0.6 mm^2. The current density within this area was kept at ~5$\mu A/mm^2$. The exposures were done at 6.6 x 10^{-5} Pa of water vapor pressure with no other detectable contaminant in the system, and all the exposures were 40 hours long. The electron beam exposed samples were analyzed using the same techniques as described above. In addition X-ray Photoelectron Spectroscopy (XPS) was used to determine the surface chemistry inside and outside the exposed area. Reflectance maps at a fixed wavelength were collected on all exposed samples with the beam spot size of about 300 x 50 μm^2, which was sufficient to resolve the exposed area. Auger electron spectroscopy was used to identify the elemental composition and to perform depth profiling. An ion beam sputter source was used to remove less than one

monolayer of material from the surface at a time during continued monitoring of the composition and chemistry of the multilayer and the chemical composition was plotted as a function of sputtering time and calibrated against known multilayer period.

3. DATA AND RESULTS

The effect of different capping layers is clearly demonstrated in their initial reflectivity, as shown in Figure 2 (unexposed values). Among the five samples, Preparation 7 has the highest pre-exposure reflectivity (66.7%) and Preparations 4 and 5 have the lowest pre-exposure reflectivities (~64%). We noticed two factors that affect the reflectivity results. The initial reflectivity is sensitive to the chamber base pressure. Since the main contaminant remaining in the chamber is usually H_2O, it is of no surprise that a slightly lower base pressure leads to slightly higher reflectivity. For example, the samples with the chamber base pressure at ~2.6 x 10^{-5} Pa had as much as 0.5% lower reflectivity than the samples with the same design made with the chamber base pressure at ~1 x 10^{-5} Pa. We also observed that the reflectivity of Ru-capped multilayer mirrors changes with time. Measuring the same multilayer mirror over a period of one year showed that the reflectivity drops as a function of time (Fig. 3). Ru-capped multilayer (Preparation 1) shows the highest reflectance drop in the first few weeks after the multilayer deposition, similar to what was observed on Si-capped multilayers [17]. A relatively small fraction of the reflectivity drop (>0.5%) is probably due to atomic re-arrangement on the interfaces within the multilayer that also leads to a small (0.02 nm) wavelength shift. The second contribution to reflectivity loss is likely due to surface contamination and oxidation. As shown in Figure 3, the major reflectance drop occurred in the first 2 months after the deposition followed by a slower degradation process. The data set covers a period of one year. Apart from the small initial wavelength shift there were no subsequent changes in the peak wavelength and peak width. The multilayers were aged in the air, kept in a plastic container and were not cleaned between the measurements. All unexposed reflectivity values in Figure 2 refer to multilayers aged in the air for at least 2 months. These multilayers presumably reached a steady-state reflectivity before they were tested for oxidation resistance. It is interesting to note that the reflectivity of Preparation 7 was initially as high as 68.3%, when measured immediately after deposition, thus comparable to or even exceeding the reflectivity of Si-capped multilayer of the same design. In Figure 3 we also plot results obtained on Si-capped multilayers [17], which are believed to be stable in the

air. However, as shown in Figure 3 Si-capped multilayers exhibit similar decrease in reflectivity as a function of time as Ru-capped ones when aged in air.

The reflectivity of multilayer coatings also strongly depends on the HSF roughness of the substrates. Ideally this roughness is 0.1 nm or less, which was the case for the substrates used in this study. On such smooth substrates multilayer coatings typically add roughness only in the HSF range, while mid- and low-spatial frequency roughness is only replicated. Atomic force microscopy (AFM) is a non-destructive technique that measures HSF roughness of the top surface, i.e. capping layer, of the multilayer coatings. Different preparations show basically identical HSF roughness (~0.18 nm) within the measurement error of ± 0.02 nm (Table 1). Roughness changes of the top layers are not directly related to reflectance, but are indicative of microstructural stability.

The microstructure of Preparation 1 sample has been studied with TEM in cross section and in plan view. A typical TEM image of cross section sample is shown in Figure 1a, where the bright layers are amorphous Si layers (Si L), and the dark layers are Mo layers (Mo L) and Ru capping layer (Ru CL). All reflection rings in the selected area diffraction (SAD) pattern of Preparation 1 sample obtained from the region including both the Ru CL and Mo/Si multilayers in the cross section match with crystalline Mo metal of body center cubic (bcc) lattice (Fig. 1b). Figure 1c is a SAD pattern taken from the area containing Si wafer and Mo/Si multilayers, in which the reflection spots come from the single crystal Si(100) wafer and the reflection rings come from the polycrystalline Mo layers. The strong intensity reflection segments shown in ring pattern (Figs. 1b and 1c) indicate that the crystalline, metallic Mo layers have a preferential orientation. Their {110} crystal planes tend to be parallel to the surface of the substrate (Si(100) wafer). This conclusion has been further verified by high resolution TEM (HRTEM) observation (Fig. 4). No diffraction rings or spots due to Ru (Fig2. 1b and 1c) are clearly distinguished. The apparent absence of a Ru signal is a sensitivity limitation. There is only one Ru layer in the whole multilayer and the thickness of this layer in cross section is only ~3 nm. In the dark-field TEM imaging mode, the objective aperture is used to select certain reflection to form an image. The dark field image thus reveals which regions of the specimen contribute to the reflection beams, and hence, is useful for identifying crystallites of a particular orientation. An objective aperture was placed on a part of the Mo{110} reflection ring, as marked by a circle on the electron diffraction pattern inserted in Figure 5 to characterize the grain size and population of crystalline Mo and Ru grains. Mo{110} reflection ring is coincident with Ru{10-10} and Ru{0002} reflections. Therefore, Figure 5 shows bright grains within the multilayer (Mo grains) but also in the last layer (Ru

capping layer) shown in the middle of the image. This implies that the Ru layer is polycrystalline and that Ru grains also show preferential orientation in either Ru(10-10), Ru(0002) or a combination of these two because these orientations have the closest match with Mo(110) d-spacing. The d-spacing for Mo(110) is 0.222 nm, for Ru(10-10) is 0.230 nm and for Ru(0002) is 0.214 nm.

A cross section HRTEM image of Preparation 1 shows lattice fringes due to crystalline Ru capping layer and Mo layers (Fig. 4). While the image in Figure 4 indicates that Mo grains have their {110} crystal planes parallel to the surface of the substrate, which is consistent with the result from electron diffraction analysis (Fig. 1b), the Ru grains in the capping layer also have a certain preferential growth orientation. The spacing between the lattice fringes or d-spacing on a crystal in Ru CL shown in Figure 4 is ~0.23 nm relative to the 0.22 nm of Mo(110). This d-spacing is characteristic of Ru(10-10) crystal orientation. However, this result is ambiguous since Ru(0002) crystal orientation. However, this result is ambiguous since Ru(002) has an almost identical d-spacing (0.214 nm).

In order to determine the preferential grain orientation and grain size of the Ru capping layer from a statistically representative data set, one needs plan-view sample observations. The plan view TEM sample preparation is very challenging since the layer of interest is a very thin, top, capping layer. This layer is affected by contamination and re-deposition during TEM sample preparation (ion beam milling). A specimen of Preparation 1 sample was prepared by thinning the sample from the back, from the Si wafer side. Another plan view sample was prepared by depositing Ru capping layer on the top of a diffusion barrier deposited on an amorphous Si layer. In this sample all three layers were coated on a TEM transparent Si_3N_4 membrane using exactly the same deposition parameters and the same layer thicknesses as for Si wafer supported sample. The advantage of this approach is that the sample does not require any sample thinning. This eliminates ambiguity due to TEM sample preparation, provides a sample with uniform thickness, allows imaging of a huge area as compared to the standard TEM wedged sample and reduces the cost for TEM imaging. A dark field TEM image of plan view sample is displayed in Figure 6. All diffraction rings in the SAD patterns on a membrane supported sample can be identified and correspond to crystalline metal Ru (Figs. 7a and 7b). The SAD pattern (Fig. 7a) was taken with an incident electron beam exactly perpendicular to the support membrane, i.e. perpendicular to the Ru capping layer. The intensity distribution over each ring is uniform under this condition. A sharp and the strongest reflection ring at 0.235 nm is due to Ru(10-10), and a broad diffuse one at 0.205 nm corresponds to Ru(10-11) overlapping with Ru(0002). We can also clearly identify a ring at 0.158 nm due to Ru(10-12) and at 0.137

nm due to Ru(11-20). Another weak ring at 0.087 nm corresponds to Ru(21-31). When the specimen is tilted relative to the incident electron beam, the intensity distribution on the reflection rings changes. SAD pattern in Fig. 7b was taken with the specimen tilted ~20° relative to the orientation in Fig. 7a. Comparing these two SAD patterns we observe that one part of Ru(10-10) ring shows a change in intensity while the other part of the ring remains similar in intensity. However, the intensity of originally weak and broad ring due to Ru(10-11) becomes strong and sharp. The intensity increase of Ru(10-11) is linked to the intensity decrease of Ru(10-10), as indicated by arrowheads in Fig. 7b. This is a strong indication of textured structure formation, i.e. the crystal orientation of Ru grains is not random.

Figure 8 is a schematic of a hexagonal close packed (hcp) Ru unit cell, where all six crystal planes identified in the electron diffraction pattern (Fig. 7a) are shown with different colors. If the incident electron beam is parallel to the c-axis of Ru unit cell (Beam-I, Fig. 8) the corresponding electron diffraction pattern will display a very strong intensity of Ru(10-10) reflection ring as is the case in Fig. 7a. In comparison X-ray powder diffraction of randomly distributed Ru grains displays the strongest reflection ring intensity (100%) for Ru(10-11) and 40% intensity peak for Ru(10-10). The uniform intensity distribution on the Ru(10-10) ring indicates that the Ru grains have random rotation along their c-axis. Tilting the Beam-I by 20° (from the full line to the dot line arrowheads direction, Fig. 8) is equivalent to tilting the specimen relative to the incident beam. Some Ru(10-10) crystal planes are then off Bragg diffraction condition and correspondingly their reflection intensity decreases. On the other hand more Ru(10-11) crystal planes meet Bragg diffraction condition and hence their reflection intensity increases. This is consistent with our experimental results (Figs. 7a and 7b). If the incident electron beam is perpendicular to Ru(10-10) crystal plane (Beam-II, Fig. 8) the corresponding electron diffraction pattern should give a notable Ru(0002) reflection ring, which was not observed in this study. Therefore, high intensity (10-10) reflection indicates that the signal is mainly due to Ru(0001) crystal plane parallel to the specimen surface. The difference in the nominal (0.214 nm) and measured (~0.23 nm) d-spacing of Ru(10-10) is likely due to lattice relaxation because the as-deposited Ru layer is so thin (~ 3nm) and located on the top of the specimen.

The grain size was determined from statistical analysis of 112 Ru grains from dark field image obtained on back-thinned sample, similar to the image shown in Figure 6. The average Ru grain size obtained from such a sample is 3.5 nm. Independently, the grain size was determined from the SAD pattern taken on the membrane supported sample

by using a select area aperture of 20 μm in diameter, in which about 1.1×10^8 Ru grains were included. Interestingly, the average Ru grain size in this sample is also ~3.5 nm.

Surface chemistry was studied using PHI Quantum 2000 XPS systems at LLNL. XPS data is quantified using relative sensitivity factors and a model that assumes a homogenous layer. Photoelectrons are generated within the X-ray penetration depths (many microns), but only the photoelectrons within the top three photoelectron escape depths are detected. Hence, the analysis depths were estimated to be 5 to 10 nm. Spectra are usually energy calibrated using the C 1s signal. This could not be performed in the spectra studied here due to the interference between the Ru $3d_{3/2}$ and C 1s peaks. Thus the spectra were charge shifted to the Si 2p signal, with a binding energy of 99.3 eV for elemental Si. Initially, the survey spectra were collected from each sample in the exposed and unexposed areas. Final collection of high resolution spectra were performed only for the elements found in the survey spectra. We used the O 1s and Ru 3p peaks to obtain chemical state information especially about the oxides. No H, He or Ar was detected in any of the samples. The two major detected elements were Ru and O. Low levels of N, Si and Mo were present as well. The presence and concentration of C on the sample was difficult to determine due to severe interference with the Ru $3d_{3/2}$ signal. Figure 9 is an example of high resolution spectra of O 1s, Ru 3d, Ru $3p_{1/2}$, Mo 3d, Si 2p and N 1s XPS peaks for Preparation 1 in the electron-beam exposed and unexposed areas. With the exception of N all other elements show well resolved peaks.

3.1. Oxidation Resistance Testing

Electron beam exposures have been successfully used in the past to study lifetimes of multilayer coatings for EUVL. We have demonstrated that accelerated electron beam exposures produce comparable damage to multilayers for accelerated EUV light exposures done in the same environment [6-7]. For the purpose of screening the capping layer preparations, we decided to test the multilayers under only one environmental condition using an electron beam as the source of energy. The exposures were done in an Auger microprobe chamber using 1 keV electrons, $5\mu A/mm^2$ current density and $6.6x10^{-5}$ Pa water vapor. The total exposure time on each sample was 40 hours.

For Preparation 1, the major changes occur in energy position, peak separation and peak shape of O 1s, Ru 3d and Ru 3p peaks. The O 1s peak in the unexposed area could be fitted with two non-linear least square curves, one

centered at 529.4 eV and the other at 531.2 eV (Figure 10a). The energies of these peaks are characteristic of the oxides RuO_2 and RuO_3, respectively. Both peaks have similar areas. In the exposed area, the fitting of O 1s peak required three non-linear least square peaks centered at 529.0 eV, 530.9 eV and 533.6 eV (Figure 10b). The peak at 529.0 eV (RuO_2) is almost twice as large as the one at 531 eV (RuO_3), indicating preferred formation of RuO_2 over RuO_3 during oxidation with water. The O 1s peak at 533.6 eV in the exposed area is due to Si oxide (SiO_{2-x}). The non-linear least square fits of the O 1s peak for Preparations 4, 5, 6, and 7 (not shown) in both the unexposed and exposed areas required three instead of two Gaussian shaped peaks, indicating the presence of Ru and Si oxides in both areas for all of these preparations. The energies of these three peaks are approximately the same but their ratios for each fit are different.

The corresponding Si 2p peak for Preparation 1 has a large elemental peak at 99.3 eV, and a smaller, wider peak near 102 eV, which again corresponds to a small amount of SiO_{2-x} (Figure 9). The Si oxide peak appears in the unexposed area of all multilayer preparation samples, but it is considerably smaller than the elemental Si peak for Preparations 1, 6, and 7. For preparations 4 and 5, the Si 2p peaks corresponding to elemental Si and Si oxide have nearly equal areas, indicating that the capping layers formed with the $Ar:N_2$ mixture preparations have reduced oxidation resistance. Since the samples were aged in air for at least 2 months before reflectivity and XPS measurements, it is expected that there was some diffusion of O and Si into the capping layer during exposure to the air, and although not measured with XPS, the Si in the as-deposited state was probably much less oxidized than the Si after aging.

The Ru $3p_{1/2}$ peak does not suffer from interference with other elemental peaks (unlike Ru $3d_{3/2}$, which interferes with C 1s). The fits to the exposed and unexposed area spectra each require two peaks, one near 483.5 eV, which includes both Ru and RuO_2, and one near 485.9 eV for RuO_3 (Figure 11a and 11b). The size of the Ru oxide component relative to the elemental Ru component is increased for the exposed area spectrum. This indicates further oxidation of the Ru capping layer with exposure. In addition, although the Ru 3d peaks are not fit, the significant reduction of their intensity in the exposed area relative to the unexposed area indicates an increased coverage of oxide. This is because an oxide layer would reduce the intensity of underlying layers due to the limited escape depth of the photoelectrons (5-10 nm).

The Si 2p peak is very similar in the exposed and unexposed areas for Preparation 1, indicating very little further oxidation of the Si. The O 1s and Ru $3p_{1/2}$ results also are consistent with oxidation of the Ru but not the Si in

the exposed area. Preparation 6 had similar O 1s, Ru $3p_{1/2}$, and Si 2p spectra to Preparation 1, indicating good oxidation resistance of the Preparation 6 capping layer and additional RuO_2 formation as well. Preparation 7 had a large increase of the Si oxide component of the Si 2p peak, and preparations 4 and 5 had smaller increases, indicating that the oxidation resistance of capping layers formed using these three preparations is reduced relative to those formed using Preparations 1 and 6. While Preparation 7 (Ru capping layer with carbon) was more resistant to oxidation from aging in the air, it was much less resistant to oxidation from electron beam plus water exposure.

For all preparations, the Mo 3d peak is unchanged in the unexposed and exposed areas, and is characteristic of metallic Mo with no Mo oxide formed. This indicates that for all preparations the oxidation does not extend as far as the first Mo layer, which is beneath both the capping layer and the first Si layer (Figure 9).

The N 1s spectra have also been obtained for all capping layer preparations. The N 1s spectra for Preparations 1 and 7 are quite weak and are due to residual N_2 in the deposition chamber, since N_2 was not deliberately used in these preparations. Preparations 4 and 5 exhibit a rather strong N 1s peak in both the unexposed and exposed area. This is expected since the capping layers for Preparation 4 and 5 were deposited in an Ar:N_2 environment, so some incorporation of N could occur. For preparation 6, the N 1s peak is strong in the unexposed area but disappears in the exposed area. This suggests that nitrogen was weakly absorbed on the capping layer surface during the post-deposition N_2 exposure of the Preparation 6 surface in the deposition chamber.

Lastly, Auger depth profiling was performed to determine interface sharpness and thicknesses of the oxide, the capping layer, and the multilayer. Auger depth profiling was performed only on Preparations 1 and 6. Figure 12 shows the results of Preparation 1 in the unexposed and exposed areas, respectively. The Auger depth profiles in the unexposed and exposed areas are strikingly similar. The underlying well-defined Mo/Si multilayer (depth greater than 7.0 nm) is unaffected by the electron beam exposure, as is the shape of the Ru, Mo, and Si profile in the layer between 1.5 nm and 7.0 nm. Oxygen is observed only in the top 1.0-1.5 nm of Ru of the exposed area, and only in the top 0.5 nm of the unexposed area. There is some diffusion of Si and Mo into the Ru capping layer as well, which may account for the observation of oxidized Si in the unexposed and exposed areas of O 1s and Si 2p XPS data. The underlying Si in the multilayer clearly is not oxidized. Preparation 6 has a very similar depth profile to Preparation 1 in terms of the depth of the oxygen into the Ru capping layer and the lack of disturbance of the underlying multilayer.

3.2. Thermal Testing

Thermal tests were performed to study the effect of temperature on different preparations. The projection optics is extremely sensitive to any change in the temperature. The temperature in the projection optics box will likely be maintained at room temperature within a fraction of a degree. However, knowledge about the thermal stability of capping layers is of interest because optics could be potentially cured at higher temperature to relieve stress or stabilize the multilayer performance [18]. Samples with different capping layer preparations were annealed at 100°C for 1 week and 200°C for 30 minutes. The annealing temperatures were controlled within ± 5°C and all experiments were performed in relatively good vacuum (base pressure ~$4x10^{-5}$ Pa). We monitored changes in period thickness, interface roughness, inter-diffusion, EUV reflectance and surface roughness.

The wavelength, which was about 13.4 nm in as-deposited samples shifted to ~13.35 nm after the samples were exposed to 100°C for 1 week. The wavelength of the multilayers exposed to 200°C for 30 minutes changed from 13.4 nm to ~13.28 nm. The data clearly show that the peak wavelength shifted by the same amount on all samples. This attests that the multilayer structures, excluding the capping layer, were the same and that the annealing conditions were very reproducible. As expected, samples annealed to 200°C for 30 minutes show a larger shift in the peak wavelength than samples annealed at 100°C. Annealing at 100°C causes about 1% drop in reflectivity in all samples except in Preparation 7 sample, where the reflectivity loss is about twice as much (Table 2). Testing at higher temperature (200°C) shows good thermal stability of Preparations 1, 4 and 6 with about ~1.7% reflectance loss. Preparation 5 shows reflectance loss of 2% and Preparation 7 about 3.5% reflectance loss. This suggests that differences in reflectivity are due to different capping layer preparations and that higher temperatures accelerate the mechanism that leads to reduced reflectivity. The HSF roughness is slightly increased for annealed samples as compared to as-deposited samples. However, the increase is still within the measurement error of ± 0.02 nm (Table 1). Hence, reflectance loss due to annealing can not be explained with increase in surface roughness.

4. CONCLUSIONS

The lifetime of projection optics remains high on a list of unresolved critical issues for EUVL technology. Development of oxidation resistant capping layers requires understanding of the microstructure of the capping layers and the oxidation mechanisms. We studied the effect of different preparations of Ru capping layers on their thermal and

oxidation resistance. The highest reflectivity was measured on Preparation 7 (ruthenium with carbon), which was very stable against aging in the air. However, this capping layer preparation had disappointing performance when exposed to the electron beam in water vapor and when exposed to high temperatures. In the electron beam exposed area, an increase in Si oxide was observed. Since Si layer is below the capping layer, this might suggest that the diffusion of oxygen through this capping layer is faster than in other preparations studied here. Ru capping layers deposited with Ar:N_2 sputtering gas mixture (Preparation 4 and 5) had low initial reflectivity. TEM images in these capping layers show small, randomly oriented Ru grains. Silicon underneath the Ru capping layer is partly oxidized even in as-deposited state. In the electron beam exposed areas we observe an increase in Si oxide underneath the Ru capping layer.

Preparation 1 and 6 samples show identical initial reflectivity. Preparation 6 sample was exposed to N_2 gas before taken out of the deposition chamber. Although we could see some N bonded to the surface of as-deposited sample this difference in surface chemistry as compared to Preparation 1 did not affect the performance of the Preparation 6 capping layer when exposed to the electron beam in the presence of water vapor. Preparation 1 had overall the best performance for thermal and oxidation stability and was therefore studied in most detail. The microstructure of the as-deposited sample was studied in cross section and in plan view using bright and dark field TEM imaging, SAD, high resolution imaging and energy-dispersive X-ray spectroscopy. The electron beam exposed area showed no increase in Si oxide underneath the Ru capping layer, unlike what we observed in Preparations 4, 5, and 7. Our results show that Ru in Preparation 1 is crystalline with an average grain size of ~3.5 nm, and has preferential growth orientation with Ru(0001) crystal planes parallel to the specimen surface. Based on limited TEM data it appears that the Ru capping layers of other preparations have randomly oriented grains. This suggests that a crystalline layer with well developed texture, such as observed in Preparation 1, is a better oxidation barrier than a layer with randomly oriented grains, such as observed in Preparations 4 and 5.

ACKNOWLEDGMENTS

We would like to thank W. Miles Clift (Sandia National Laboratories) for Auger measurements. Cindy Larson, Cheryl Evans, Regina Soufli, Art Nelson, Rick Gross (all LLNL), Eric M. Gullikson (LBNL) and Patrick A. Kearney (now at SEMATECH) are thanked for their contributions. We also appreciate discussions and support from Stefan Wurm and

Obert Wood (SEMATECH). This work was performed under the auspices of the U.S. Department of Energy by University of California Lawrence Livermore National Laboratory under contract No. W-7405-Eng-48. Operation of the Advanced Light Source was supported by the Director, Office of Science, Office of Basic Energy Sciences, of the U.S. Department of Energy under Contract No. DE-AC03-76SF00098. This project was funded by SEMATECH under Project LITH 160.

REFERENCES

1. U. Stamm, "Extreme ultraviolet light sources for use in semiconductor lithography – state of the art and future development, *J. Phys. D: Appl. Phys.* **37** (2004) 3244-3253.
2. H. Komori, G. Soumagne, T Abe, T. Suganuma, Y. Imai, H. Someya, Y. Takabayashi, A. Endo, and K. Toyoda, "Laser-produced plasma light source development for extreme ultraviolet lithography", *Jpn. J. Appl. Phys*. **43** (2004) 3707-3712.
3. N. Benoit, S, Yulin, T. Feigl, N. Kaiser, "Radiation stability of EUV Mo/Si multilayer mirrors", *Physica* **B 357** (2005), 222-226.
4. L. E. Klebanoff, W. M. Clift, M. E. Malinowski, C. Steinhaus, S. Bajt, "Radiation-induced protective carbon coating for extreme ultraviolet optics", *J. Vac. Sci. Technol*. **B20**, 695-703 (2002).
5. N. Koster, B. Mertens, R. Jansen, A. Van de Runstraat, F. Stietz, M. Wedowski, H. Meiling, R. Klein, A. Gotwtwald, F. Scholze, M. Visser, R. Kurt, P. Zalm, E. Louis, A. Yakshin, "Molecular contamination mitigation in EUVL by environmental control", *Microelectron. Eng.* **61-62** (2002) 65-76.
6. S. Bajt, H. N. Chapman, N. Nguyen, J. Alameda, J. C. Robinson, M. Malinowski, E. Gullikson, A. Aquila, C. Tarrio, S. Grantham, "Design and Performance of Capping Layers for EUV Multilayer Mirrors," in *Emerging Lithographic Technologies VII*, R. L. Engelstad, ed., *Proc. SPIE* **5037** (2003), 236-248.
7. S. Bajt, H. N. Chapman, N. Nguyen, J. Alameda, J. C. Robinson, M. Malinowski, E. Gullikson, A. Aquila, C. Tarrio, and S. Grantham, "Design and performance of capping layers for extreme-ultraviolet multilayer mirrors", *Applied Optics* **42**, (2003).

8. B. Mertens, M. Weiss, H. Meiling, R. Klein, E. Louis, R. Kurt, M. Wedowski, H. Trenkler, B. Wolschrijn, R. Jansen, A. van de Runstraat, R. Moors, K. Spee, S. Plöger, R. Van de Kruijs, ”Progress in EUV optics lifetime expectations”, *Microelectron. Eng.* **73-74** (2004) 16-22.

9. B. M. Mertens, B. van der Zwan, P. W. H. de Jager, M. Leenders, H. G. C. Werij, J. P. H. Benschop, and A. J. J. van Dijsseldonk, “Mitigation of surface contamination from resists outgassing in EUV lithography”, Microelectron. Eng. 53, 659-662 (2000).

10. K. Boller, R.-P. Haelbich, H. Hogrefe, W. Jark, and C. Kunz, “Investigation of carbon contamination of mirror surfaces exposed to synchrotron radiation”, *NIM* **208** (1983) 272-279.

11. S. Graham, C. Steinhaus, M. Clift, and L. Klebanoff, “Radio-frquency discharge cleaning of silicon-capped Mo/Si multilayer extreme ultraviolet optics”, J. Vac. Sci. Technol., B20, 2393-2400 (2002).

12. K Hamamoto, T. Tanaka, T. Watanabe, N. Sakaya, M. Hosoya, T. Shoki, H. Hada, N. Hishinuma, H. Sugahara, H. Kinoshita, “Cleaning of extreme ultraviolet lithography optics and masks using 13.5 nm and 172 nm radiation”, *JVST* **B23** (2005), 247-251.

13. B. M. Mertens, N. Koster, R. Jansen, A. van de Runstraat, H. Werij, F. Stietz, M. Wedowski, H. Meiling, R. Klein, R. Thornagel, F. Scholze, G. Ulm, R. Kurt, P. Zalm, E. Louis, A. Yakshiun, in : ASET/SEMATECH Workshop on EUV Lithography, Matsue, 2001, O4-5.

14. A. E. Yakshin, E. Louis, E. L. G. Maas, F. Bijkerk, R. Klein, F. Scholze, P. Zalm, F. Stietz, M. Wedowski, S. Muellender, B. Mertens, H. Meiling, in ASET/SEMATECH Workshop on EUV Lithography, Matsue, 2001, P6-6.

15. S. Bajt, J. B. Alameda, T. W. Barbee Jr., W. M. Clift, J. A. Folta, B. Kaufmann, E. A. Spiller, ”Improved reflectance and stability of Mo-Si multilayers”, *Opt. Eng.* **41** (2002) 1797-1804.

16. J. H. Underwood, and E. M. Gullikson, “High-resolution, high-flux, user friendly VLS beamline at the ALS for the 50-1300 eV energy region,” *J. Electron. Spectrosc. Relat. Phenom.* **92** (1998) 265-272.

17. P. B. Mirkarimi, “Stress, reflectance, and temporal stability of sputter-deposited Mo/Si and Mo/Be multilayer films for extreme ultraviolet lithography”, Opt. Eng. 38, 1246-1259 (1999).

18. S. Bajt, in preparation.

BIOGRAPHIES

Saša Bajt recived her Pd.D. in Physics from the University of Heidelberg, Germany, in 1990. She worked for The University of Chicago at the National Synchrotron Light Source (NSLS) developing x-ray fluorescence microprobe and micro x-ray spectroscopy. Dr. Bajt was a recipient of a Hawley medal in 1999 for the innovation and application of microbeam XAFS to mineralogical research. She joined Lawrence Livermore National Laboratory in 1996 where she is leading Multilayer Technology Development Team working on lifetime issues of EUVL multilayers. Her research interests include multilayer optics for EUV and x-ray region, surface and interface science, thick multilayer growth processes and x-ray microscopy and spectroscopy.

Zu Rong Dai (Z. R. Dai) received his Ph. D. in Materials Physics from the University of Science and Technology, Beijing, in 1996. He was a Visiting Scientist at the University of Washington, Seattle (1996 to 1999) and then joined the Georgia Institute of Technology as a Research Scientist. He joined the Lawrence Livermore National Laboratory in 2003, and is currently a Career Physicist in the Materials Science and Technologies Division, the Chemistry and Materials Science Directorate. His research interests include synthesis and structural characterization of advanced materials and extraterrestrial dust particles.

Erik J. Nelson received his Ph.D. in Physics from Stanford University in 2000. He worked as a National Research Council (NRC) Postdoctoral Research Associate for the National Institute of Standards and Technology (NIST) from 2000-2001 at the National Synchrotron Light Source (NSLS) performing X-ray absorption and photoelectron spectroscopy experiments. He joined Lawrence Livermore National Laboratory (LLNL) in 2001, and is currently a member of the research staff of the Materials Science and Technologies Division of LLNL. His research interests include X-ray photoelectron and absorption spectroscopies, and surface and interface science of optical and technological materials.

Mark A. Wall received his A.S. degree in Electron Microscopy from San Joaquin Delta College in 1981. He is a microscopist in Chemistry and Materials Science Directorate at Lawrence Livermore National Laboratory. His research

interests include transmission electron microscopy studies of thin film microstructures and Pu alloys and in-situ electron microscopy.

Jennifer B. Alameda received her A.S. degree in Scientific Industrial Technology from Las Positas College, Livermore, California, in 1994. She is currently a senior technologist in the Engineering Department at Lawrence Livermore National Laboratory (LLNL). Her research interests include thin film coatings, x-ray optics and extreme ultraviolet lithography (EUVL).

Nhan Q. Nguyen received his M.S. degree in Material Science from Washington University, St. Louis, Missouri, in 1976. He is currently a System Control Engineer at Lawrence Livermore National Laboratory. His research interests include anything and everything that requires control system.

Sherry L. Baker received an Associate Degree in Electron Microscopy from San Joaquin Delta College, Stockton CA. She is an Engineering Associate at Lawrence Livermore National Laboratory. Sherry's interest is in the application of state-of-the-art metrology techniques to the development of advanced x-ray optical components and systems. Her primary focus has been the characterization of optical components implemented in the development of extreme ultraviolet lithography (EUVL).

Jeffrey C. Robinson received a certificate in Machine Tool Repair from Diablo Valley Jr. College in 1990, and a Certificate in Vacuum Technology in 1994. He is a Senior Mechanical Technician staff member at LLNL with special focus on vacuum systems and magnetron and ion beam sputtering processes for thin films.

John S. Taylor leads the X-Ray Optics and the Precision Systems and Manufacturing Groups at LLNL. He also directs LLNL's EUV Lithography Program, which designed and constructed the first wide-field diffraction-limited EUVL imaging cameras. His experience includes optical manufacturing, diamond turning, and metrology. He received his Ph.D. in Mechanical Engineering from Purdue University in 1984.

Andrew Aquila received his BS degree in Engineering Physics from the University of California, Berkeley in 2004. He has been working for the Center of X-ray Optics at Lawrence Berkeley National Laboratory since 2001. He is currently working for his PhD in Applied Science and Technology at the University of California, Berkeley.

Nora Virginia (Ginger) Edwards is a scientist at Freescale Semiconductor (formerly Motorola Semiconductor Products Sector) and is on assignment to SEMATECH in Austin, Texas. There she is the project manager for the EUV Optics Contamination and Lifetime Project. Prior to joining Freescale Semiconductor she was a Fulbright Fellow at Linkoping University in Sweden. Her areas of scientific expertise include: EUV contamination, optical properties and structure of microelectronic and optoelectronic materials, heteroepitaxy and residual stress, vacuum ultraviolet spectroscopic ellipsometry, dynamic (real-time) ellipsometry and low-temperature measurements. Ginger received her Ph.D. in Materials Science and Engineering from North Carolina State University in Raleigh, NC in 1998.

TABLES

Table 1: High spatial frequency (HSF) roughness measured with AFM on as-deposited and thermally annealed samples.

Preparation	As-deposited (nm rms)	100°C for 1 week (nm rms)	200°C for 30 min (nm rms)
1	0.187	0.195	0.198
4	0.180	0.213	0.202
5	0.215	0.207	0.200
6	0.170	0.195	0.199
7	0.173	0.195	0.178

Table 2: Reflectance loss (absolute percent) for Preparations 1-6 showing variation due to differences in capping layer structures.

Preparation	ΔR (%) for 100°C	ΔR (%) for 200°C
1	-1.00	-1.60
4	-0.80	-1.68
5	-1.05	-2.04
6	-1.07	-1.74
7	-2.10	-3.54

LIST OF FIGURE CAPTIONS

Figure 1: (a) A typical bright field TEM image of cross section sample. (b) SAD pattern from a region including Ru capping layer and molybdenum layers, in which all reflection rings are indexed by bcc Mo. (c) SAD pattern from the region including Si(100) wafer (spot-like reflections) and Mo layers (rings).

Figure 2: Initial absolute reflectivity (unexposed) ranges between 64.1% (Preparation 4) to 66.7% (Preparation 7) due to different preparation techniques. In the electron beam exposed areas (exposed) the reflectivity is always lower. The largest reflectivity drop was observed for Preparation 7 sample.

Figure 3: Reflectance change as a function of time for Ru- (circles) and Si-capped (squares) multilayer.

Figure 4: High resolution TEM image of the few top layers of Preparation 1 in cross section. Silicon layer (Si L) are amorphous and molybdenum layers (Mo L) are crystalline. Ruthenium capping layer (Ru CL) shows fringes characteristic for crystalline material.

Figure 5: Dark field image of the top few layers in Preparation 1. The image was formed by using the electrons contributed from overlapped Mo(110), Ru (10-10) and Ru (0002) reflections, as marked by a circle on the inserted diffraction pattern in the top left corner. The brighter areas are crystallites of the same orientation. Ru capping layer is the last layer approximately in the center of the image.

Figure 6: Dark field image (plan view sample) showing Ru grain size and distribution.

Figure 7: (a) SAD pattern from plan view on a membrane supported sample, taking under the condition of incident electron beam exactly perpendicular to the membrane. (b) SAD pattern from the same area after tilting the sample by ~20°. All the rings in the diffraction pattern can be identified with polycrystalline hcp Ru.

Figure 8: Color coding of different crystal planes in Ru hcp crystal structure.

Figure 9: XPS data of O 1s, Ru 3d, Ru 3 p, Mo 3 d, Si 2 p and N 1s on Preparation 1 sample. The solid lines are data from as-deposited surface and the dashed lines are from electron beam exposed areas.

Figure 10: High resolution XPS data on O 1s peak in unexposed (a) and exposed area (b) in Preparation 1.

Figure 11: High resolution XPS data on Ru $3p_{1/2}$ peak in unexposed (a) and exposed area (b) in Preparation 1.

Figure 12: Auger depth profile on Preparation 1 sample in unexposed area (dash) and in an electron beam exposed area (solid).

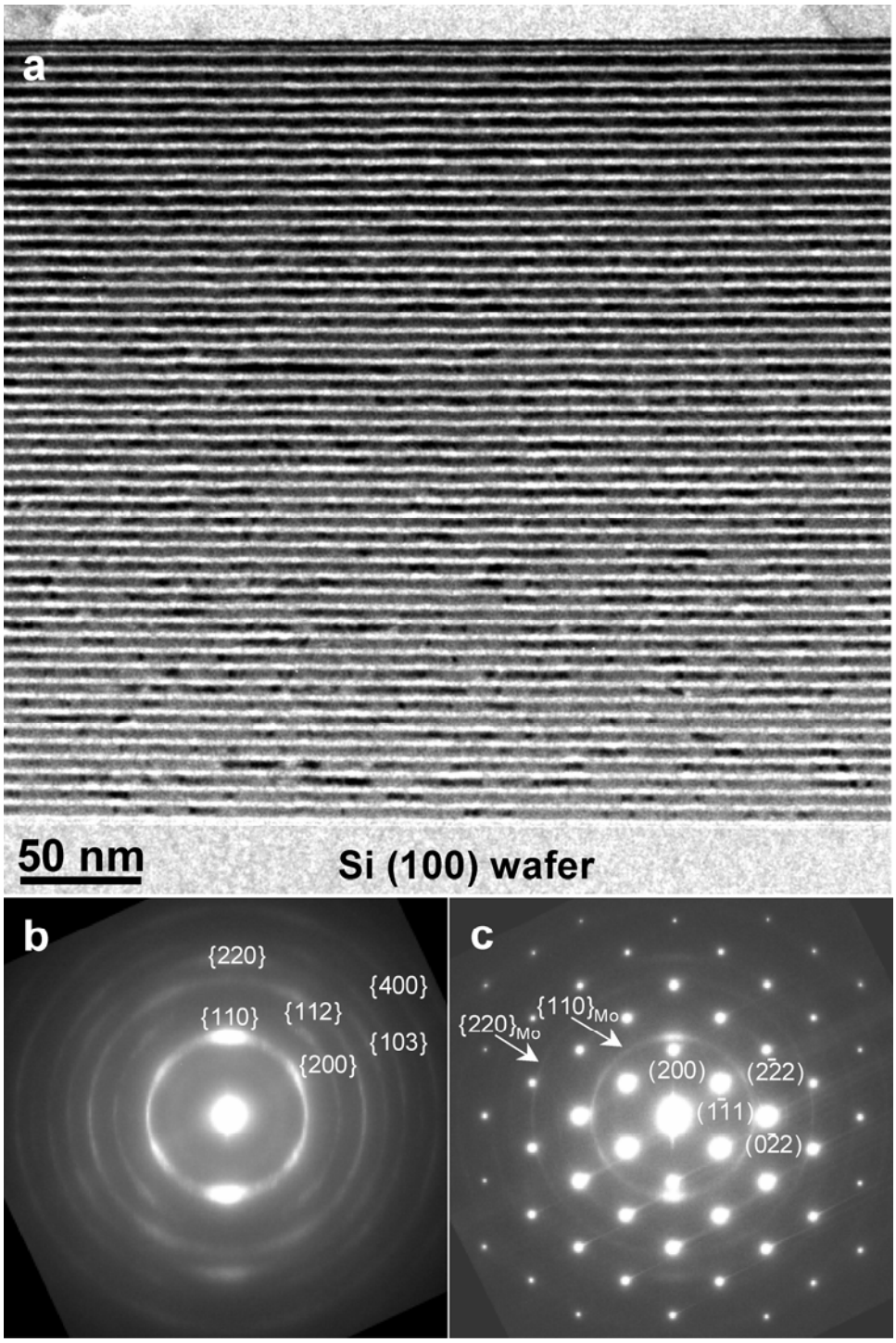
a
50 nm
Si (100) wafer
b
{220}
{400}
{110}
{112}
{103}
{200}
c
{110}Mo
{220}Mo
(200)
(2$\bar{2}$2)
(1$\bar{1}$1)
(02$\bar{2}$)

Figure 1

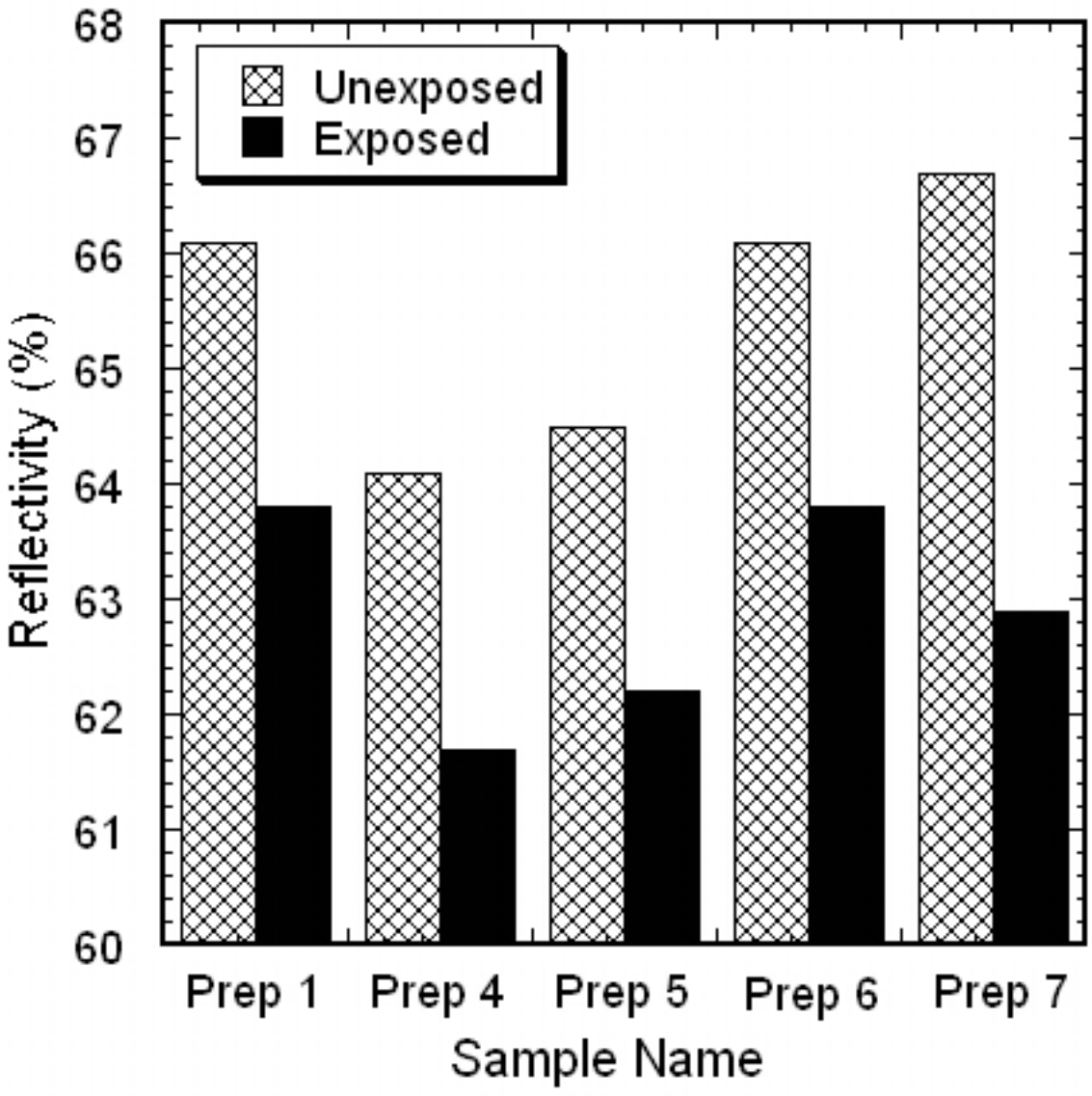
Unexposed
Exposed
Reflectivity (%)
68
67
66
65
64
63
62
61
60
Prep 1
Prep 4
Prep 5
Prep 6
Prep 7
Sample Name

Figure 2

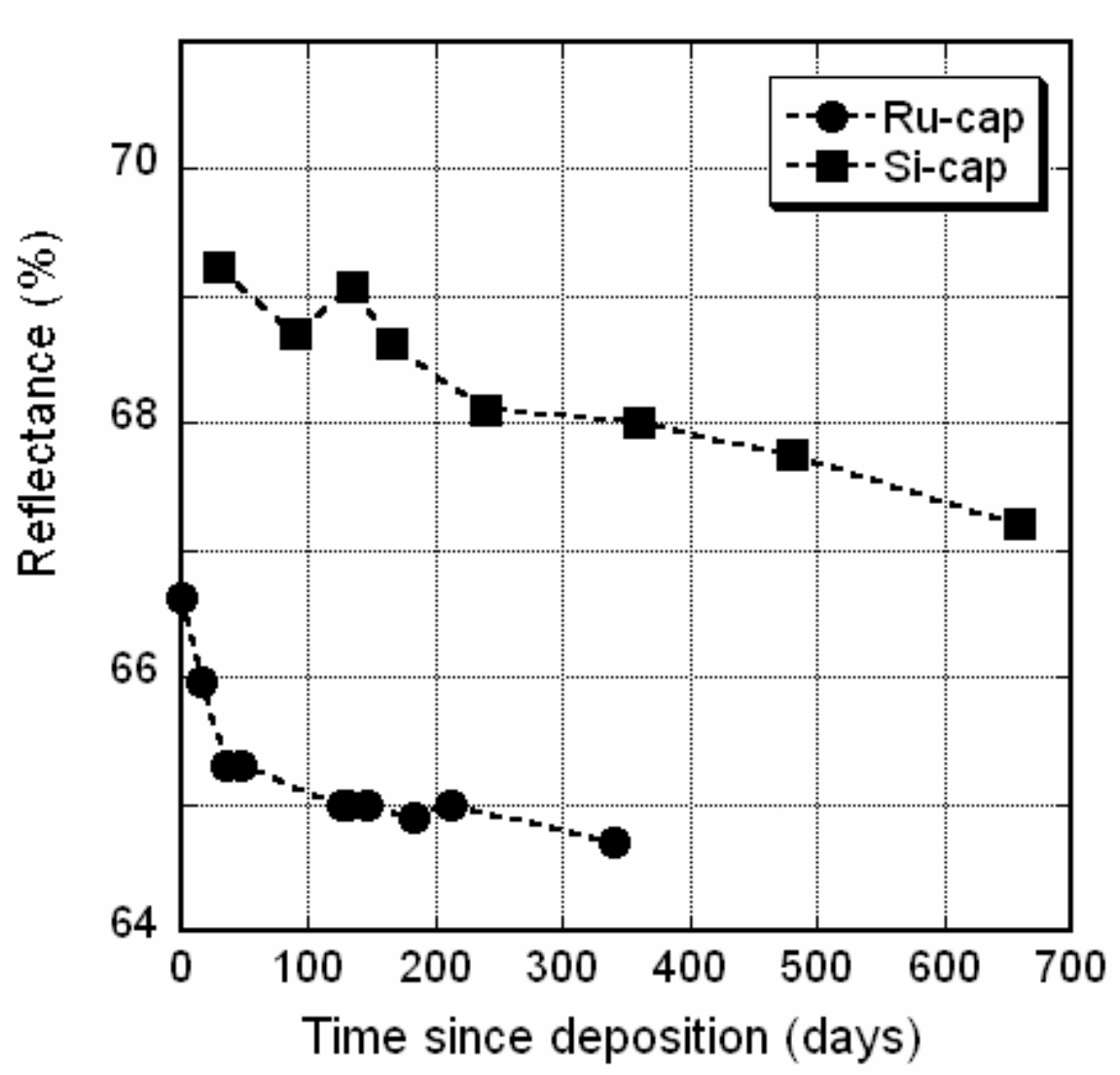
Ru-cap
Si-cap
Reflectance (%)
70
68
66
64
0
100
200
300
400
500
600
700
Time since deposition (days)

Figure 3

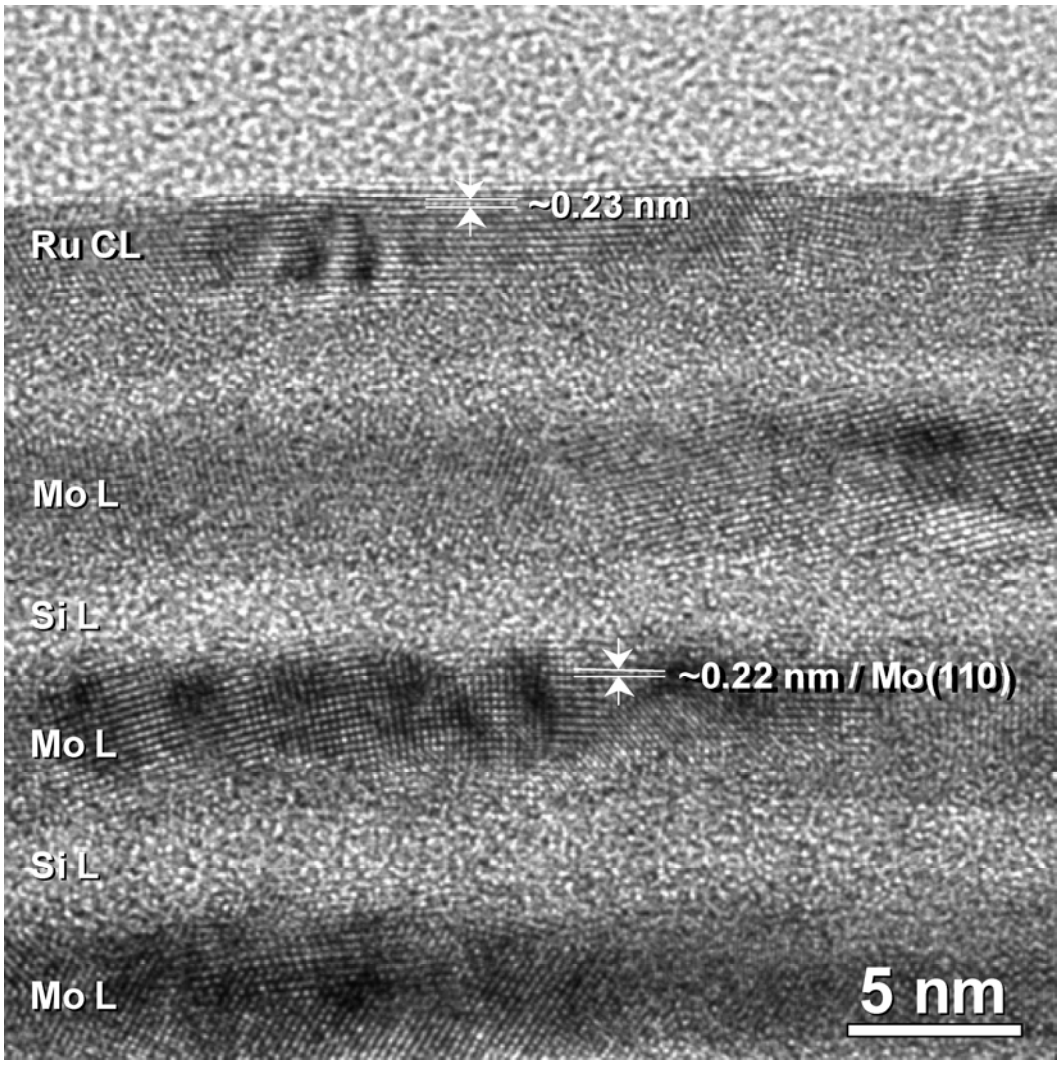

Figure 4

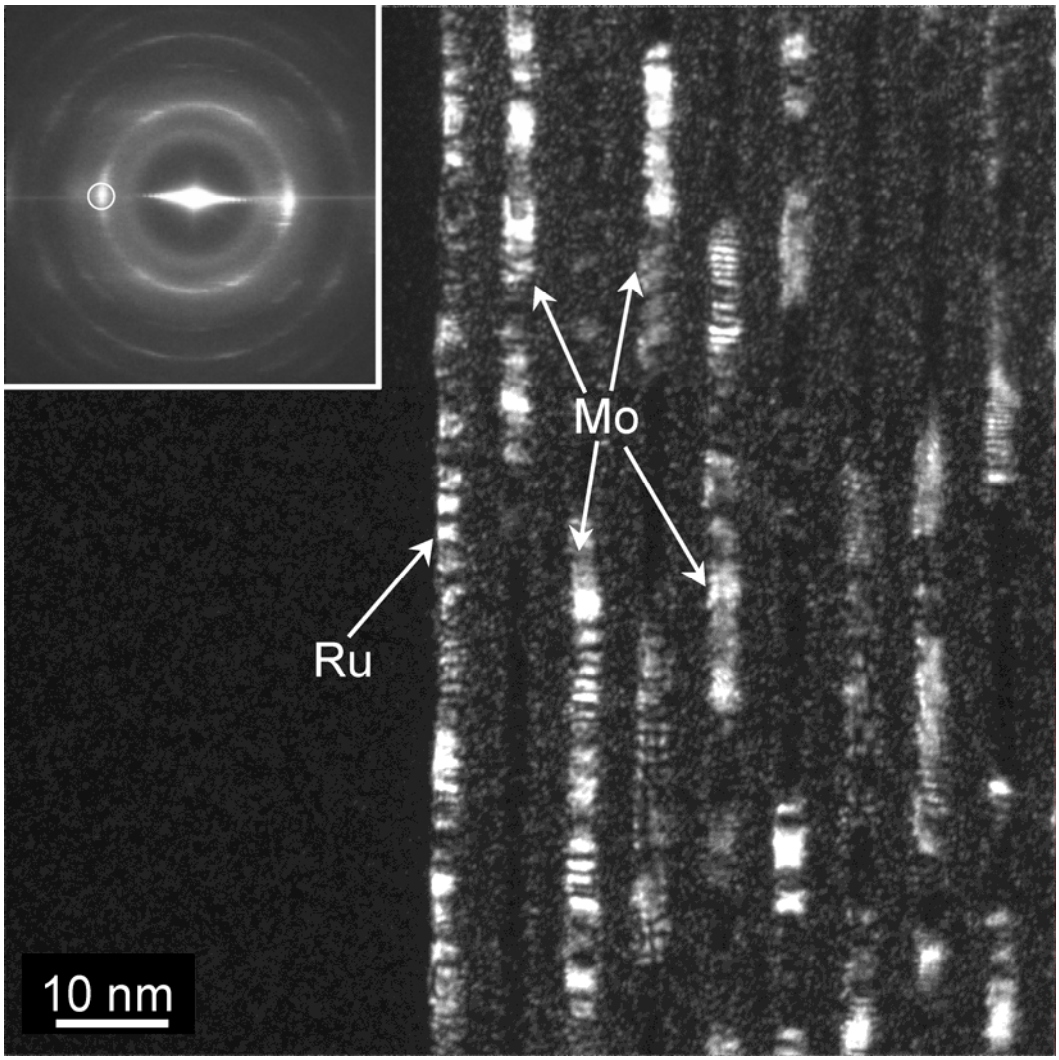

Figure 5

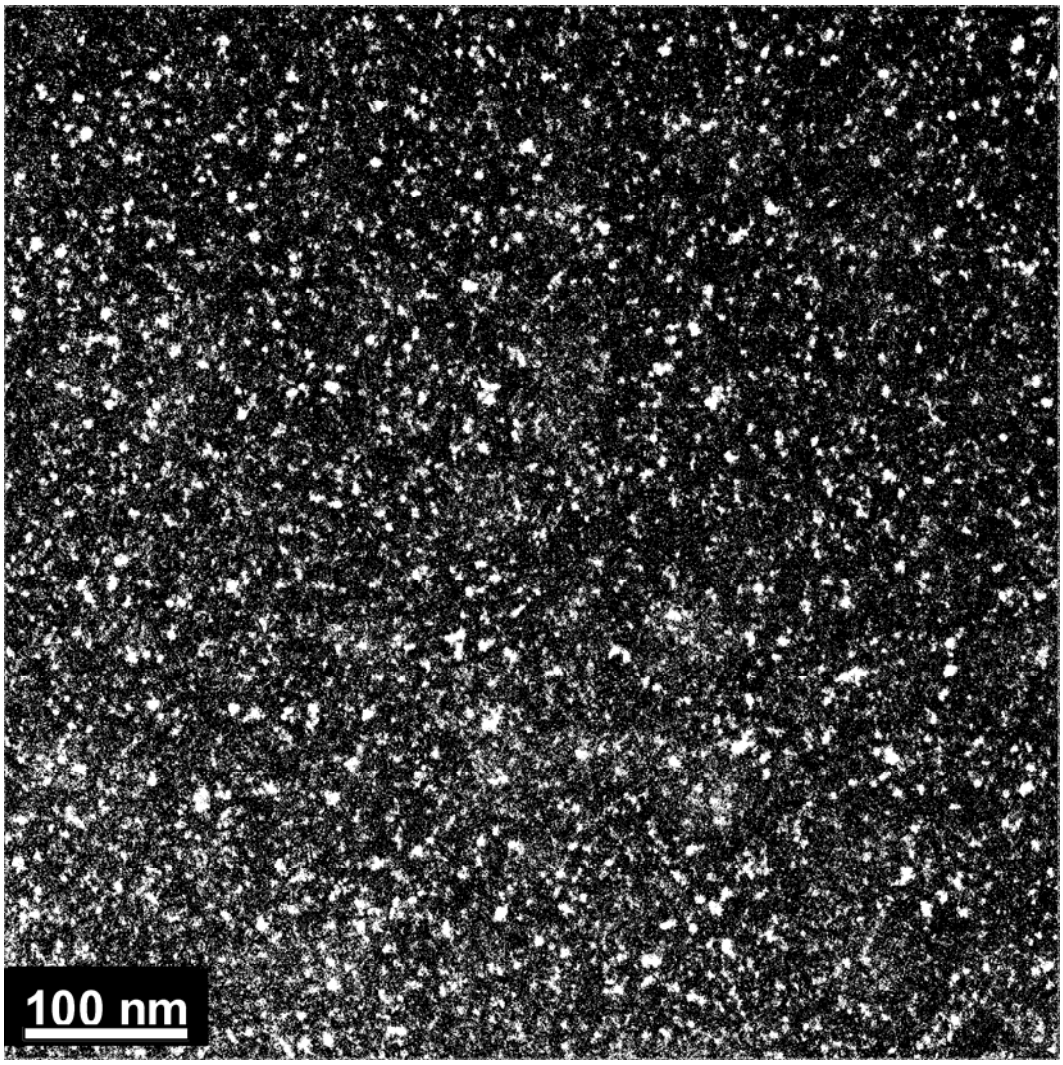

Figure 6

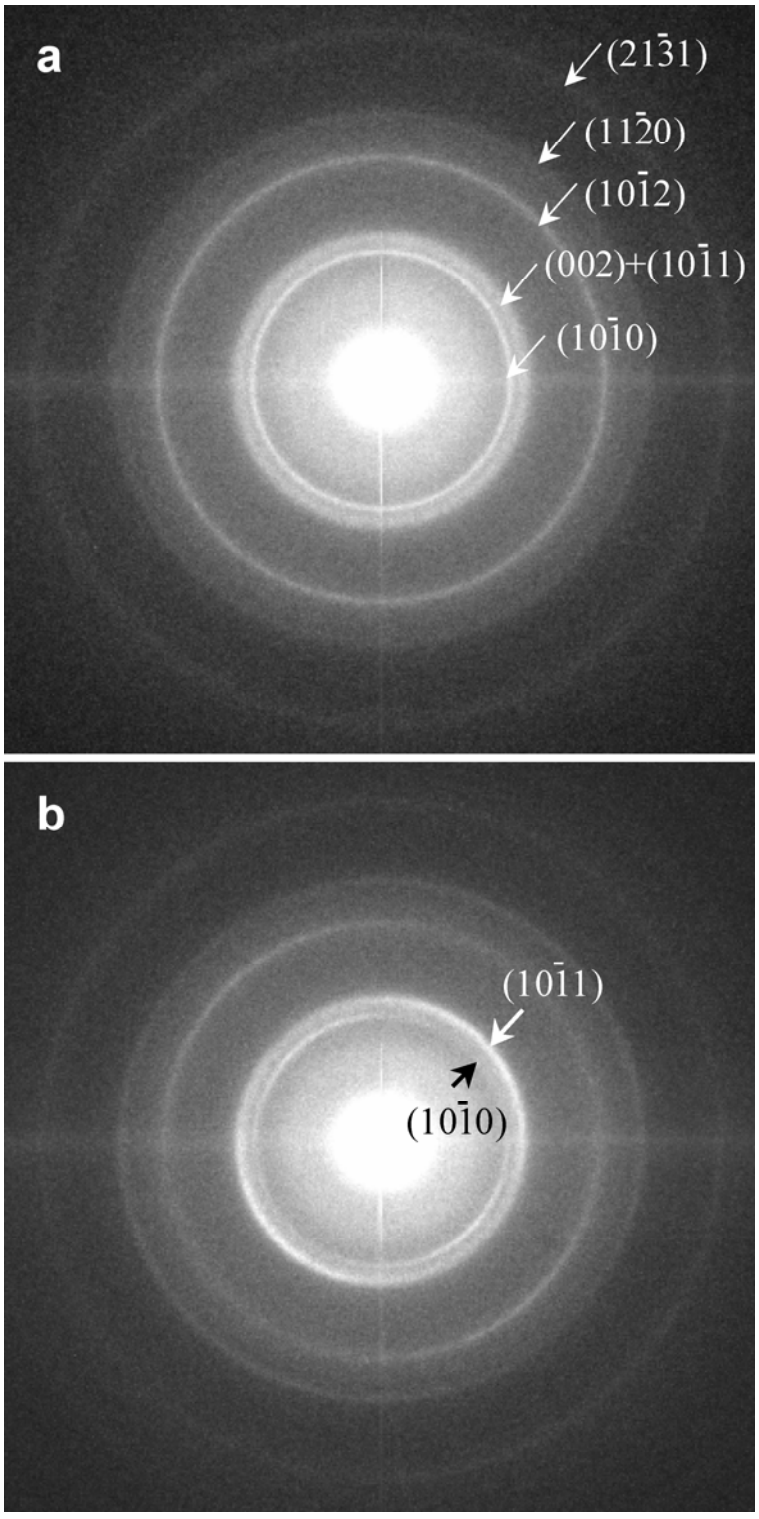

Figure 7a and 7b

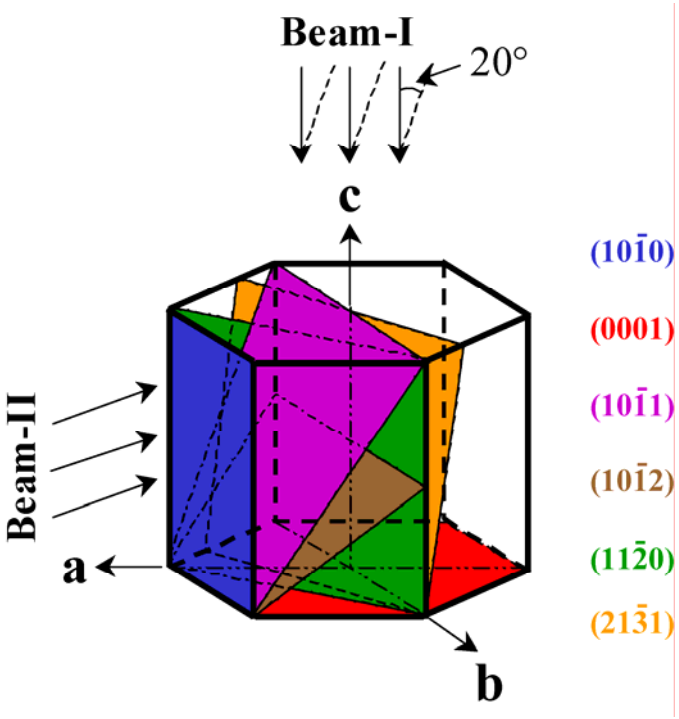
Beam-I
20°
c
Beam-II
a
b
(10$\bar{1}$0)
(0001)
(10$\bar{1}$1)
(10$\bar{1}$2)
(11$\bar{2}$0)
(21$\bar{3}$1)

Figure 8

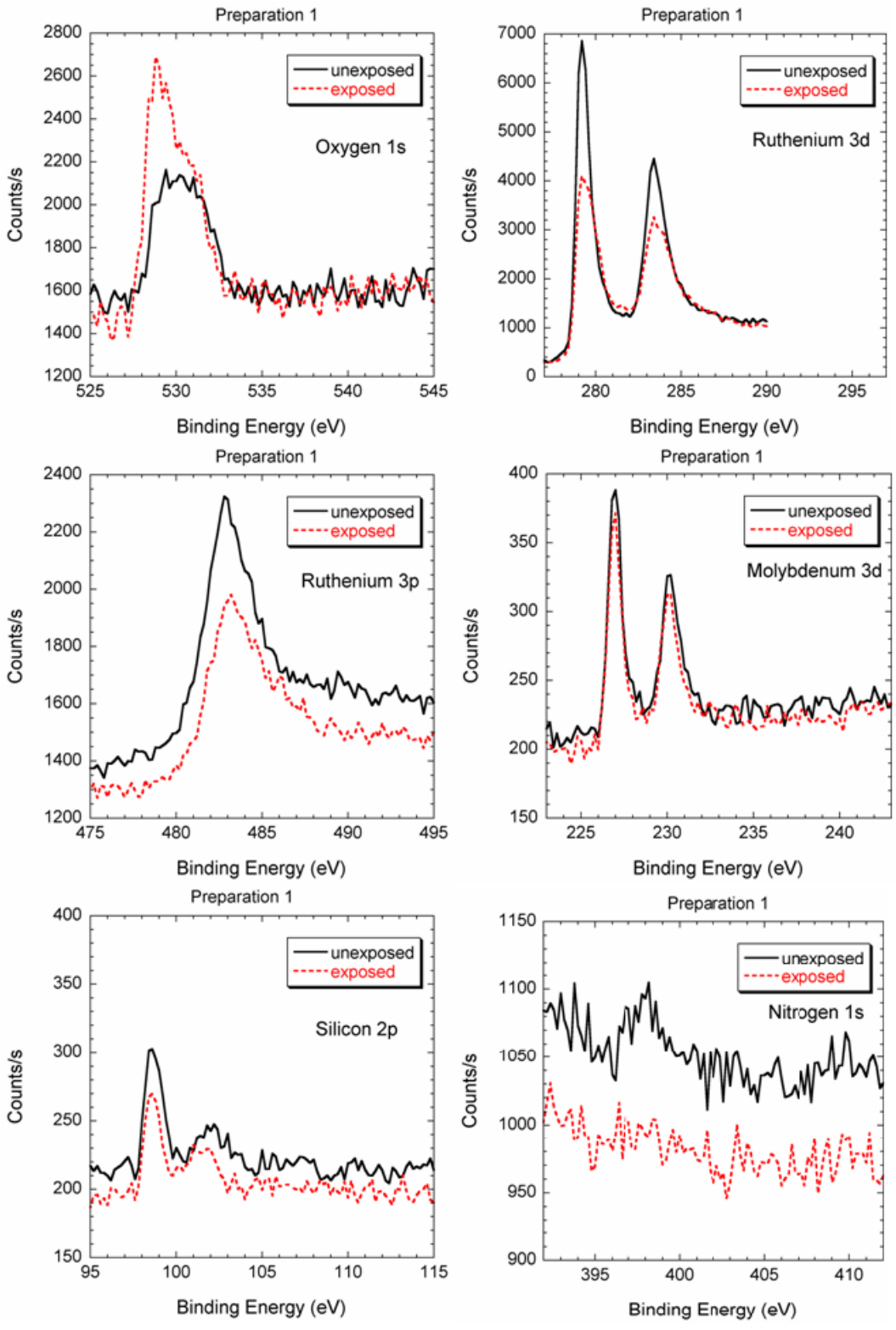
Preparation 1
unexposed
exposed
Oxygen 1s
Counts/s
Binding Energy (eV)
Preparation 1
unexposed
exposed
Ruthenium 3d
Counts/s
Binding Energy (eV)
Preparation 1
unexposed
exposed
Ruthenium 3p
Counts/s
Binding Energy (eV)
Preparation 1
unexposed
exposed
Molybdenum 3d
Counts/s
Binding Energy (eV)
Preparation 1
unexposed
exposed
Silicon 2p
Counts/s
Binding Energy (eV)
Preparation 1
unexposed
exposed
Nitrogen 1s
Counts/s
Binding Energy (eV)

Figure 9

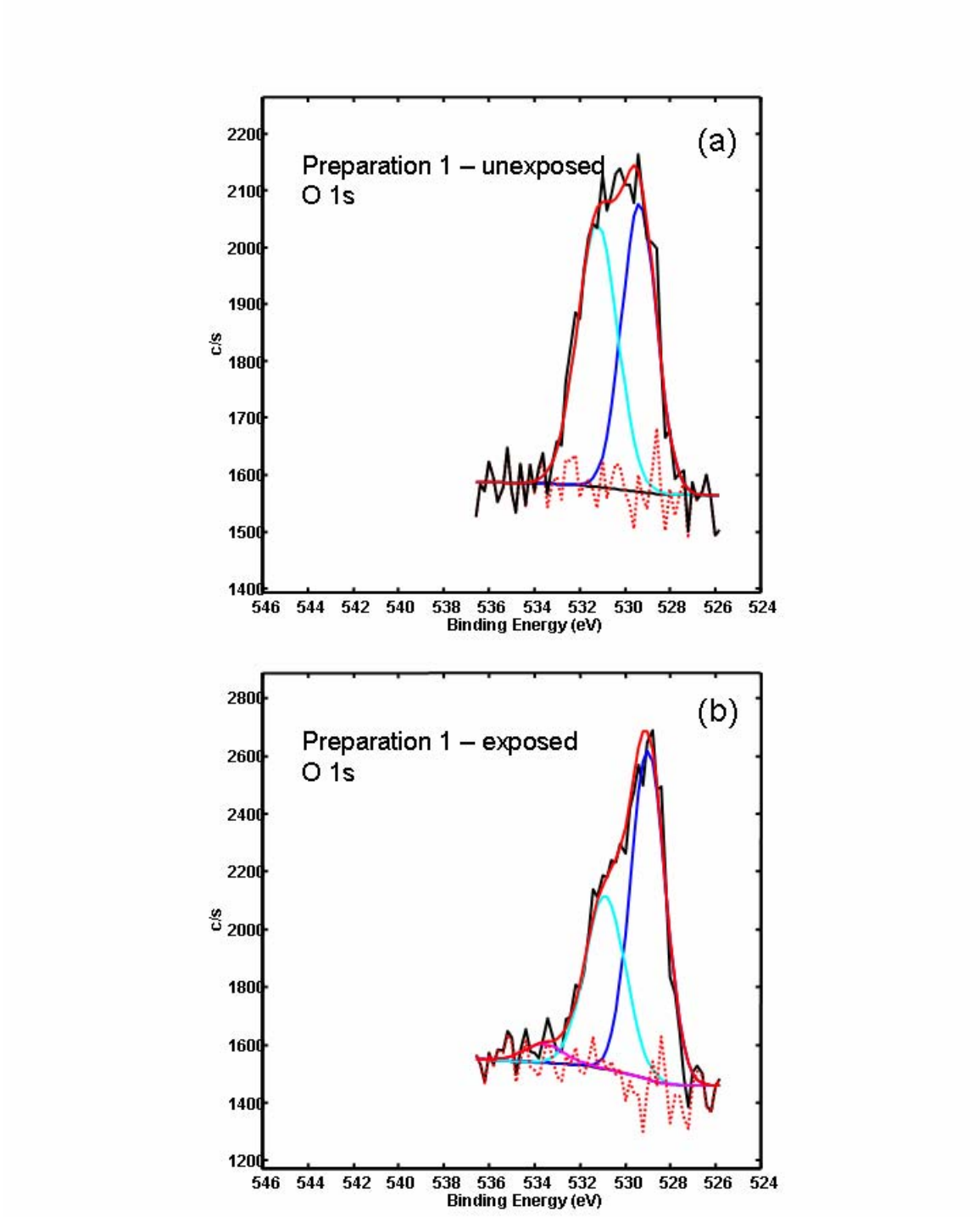

Figure 10a and 10b

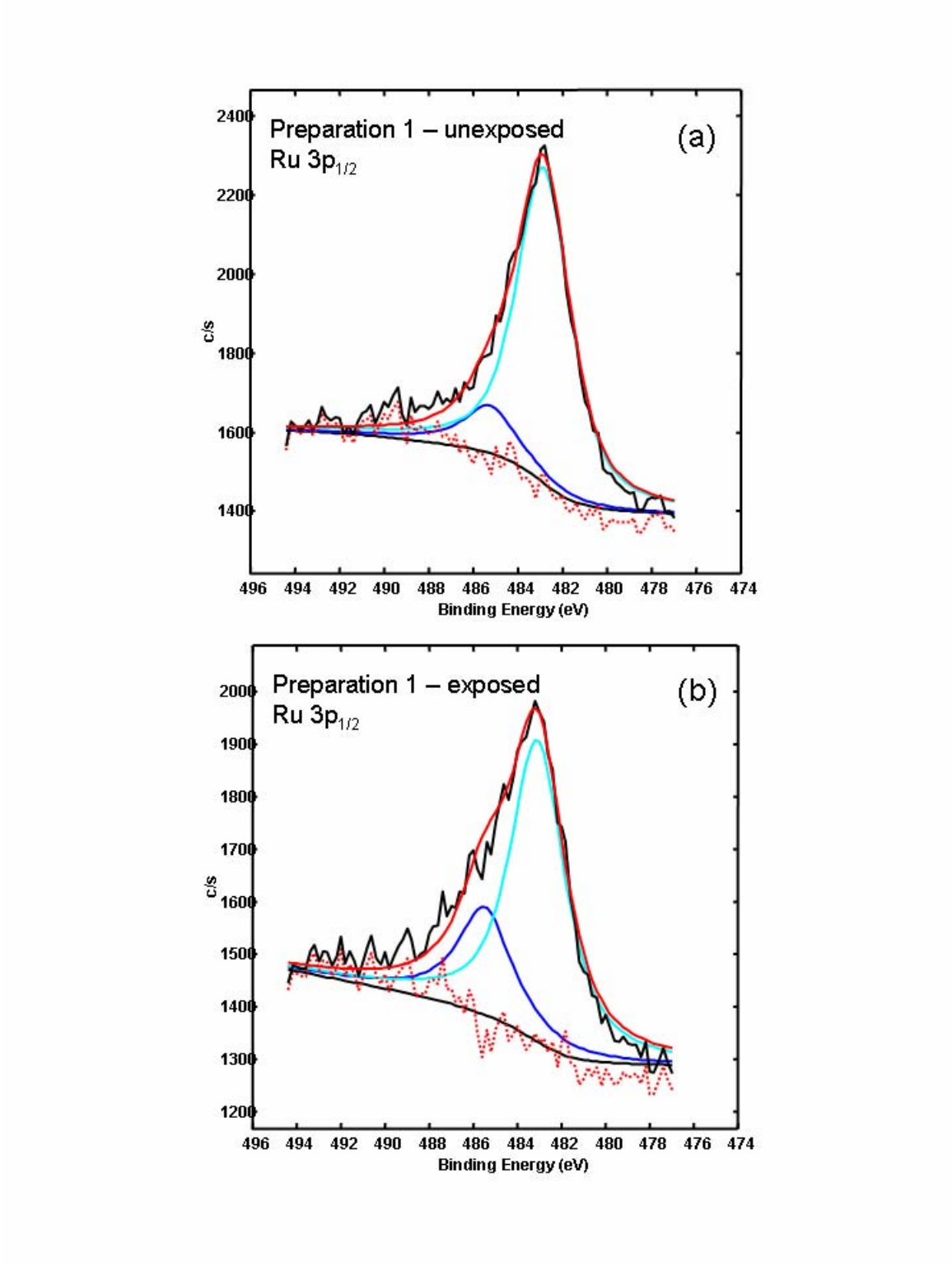

Figure 11a and 11b

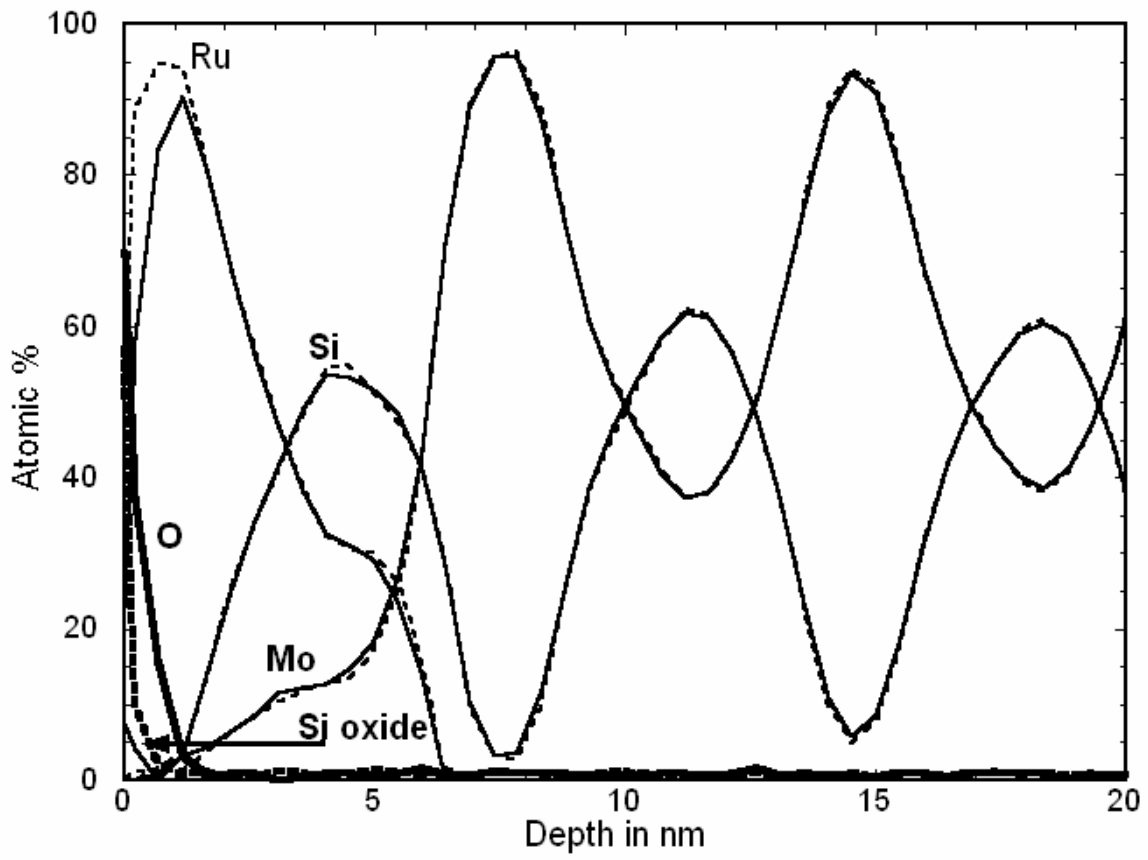

Figure 12